Supplementary Information (SI) for Soft Matter.

Supporting information

to

Controlling self-assembly and interfacial mechanics of polymer spheres and ellipsoids at fluid interfaces with surface roughness

Md Anisur Rahman and Peter J. Beltramo*

Department of Chemical Engineering, University of Massachusetts Amherst, Amherst, Massachusetts 01003, United States

* Corresponding author, email: pbeltramo@umass.edu

Contents

Other supporting materials for this manuscript include the following:

Movies S1 to S4

Supporting text

Additional Methods

Particle synthesis

Dispersion polymerization was used to synthesize linear polystyrene (LPS) seed particles to be used in subsequent fabrication of rough spheres and ellipsoids. Briefly, 0.36 g of PVP was added in a 50 mL round-bottom flask (RBF) containing 18.4 mL of IPA. In a separate glass vial, 0.05 g of AIBN (oil soluble initiator) was dissolved in 5.6 mL of styrene (monomer). The resulting solution was added to the RBF, which was then rotated for 24 h in an oil bath kept at 70 °C to initiate polymerization followed by a 5 min purging with nitrogen. Upon complete polymerization, at least five alternating centrifugation and sonication steps were conducted to remove any remaining monomer, initiator, and solvent from the LPS spheres which finally were kept suspended in water. The resultant smooth LPS spheres were either stretched thermomechanically to smooth ellipsoids[1] (see below for details) or further transformed into convex rough spheres by seeded emulsion polymerization (SEP). In the SEP process for synthesizing convex rough spheres having low (high) roughness, first, a monomer mixture in a 7.1 mL glass vial was prepared by dissolving 2.5 (5) wt % of V-65 initiator in 0.2 (0.3) mL of tBA monomer. Next, 3.2 mL of 1 wt % aqueous PVA solution was added to the monomer mixture, followed by 60 s vortexing to emulsify the mixture. Afterwards, 0.3 g LPS seed spheres suspended in 0.8 mL of 1 wt % aqueous PVA solution were added to the emulsion. To facilitate the swelling of the seed spheres with the monomer mixture, the vial was then rotated at 30 rpm for 24 h. After the swelling period, the seeded emulsion vial was immersed in a 70 °C oil bath to carry out the polymerization while rotating at 40 rpm for 24 h. Upon polymerization, the tBA monomer gets converted to poly tertbutyl acrylate (PtBA) patches which protrude from the surface of the particle. These convex rough spheres were recovered by at least six cycles of centrifugation, resuspension and sonication with water. Convex rough spheres were either used as is, stretched to convex rough ellipsoids, or further processed into concave rough spheres by acid catalyzed hydrolysis (ACH, details below).

To transform the polymer microspheres into ∼4.5:1 aspect ratio (AR) microellipsoids, our thermomechanical stretching method was used[1]. Briefly, smooth or convex rough microspheres were spread on a PVA solution contained in a rectangular Teflon mold and allowed to dry to create particle-embedded PVA film. The dried film was loaded onto a custom-built stretching apparatus and subsequently submerged into an oil bath at T = 115 °C, before being stretched to a predetermined draw ratio (2:1). The regions with desired aspect ratio microellipsoids were isolated from the stretched PVA film and then dissolved in water to recover the particles. To discard the PVA and extract the microellipsoids, at least six consecutive centrifugation-resuspension cycles were carried out.

To create concave rough particles, ACH was performed on convex rough spheres and ellipsoids to remove the convex patch (PtBA) domains by converting them to water soluble poly(acrylic acid). In a typical ACH experiment, 3 mL of TFA was added to a 7.1 mL glass vial containing 100 mg of convex particles and subsequently rotated at 40 rpm for 24 h. Afterwards, particle washing was done by at least five alternating centrifugation and sonication steps. The first wash was performed in the presence of EtOH to adjust the fluid phase density and all subsequent washes were conducted using water.

Particle characterization

Scanning electron microscopy (SEM) images of the synthesized particles were acquired via an FEI Magellan 400 XHR scanning electron microscope operating at an acceleration voltage of 1 kV. The samples for SEM were prepared on silicon wafer chips via drop casting the diluted particle suspension in water followed by evaporation of water at ambient conditions. In order to facilitate identifying the surface features, the particles were imaged without a conductive metal coating. By analyzing such SEM images of >100 particles, the diameters of the particles were measured using the open-source program ImageJ[2]. The patch diameter was obtained by measuring at least 200 patches spanning across no less than 10 individual particles. However, an accurate quantitative analysis of the surface morphology via SEM was restricted due to the minor beam damage of the PtBA domains that appears to have concave features. Therefore, atomic force microscopy (AFM) was conducted on a single particle to calculate the surface roughness. Prior to AFM, the particles were immobilized on a PDMS film via gel trapping technique[3]. In short, a 2 wt % GG suspension was prepared by introducing the required amount of GG powder into water at 80 °C, kept under continuous stirring at 1200 rpm for 2 h. The GG solution was poured into a 35 mm glass Petri dish that created an air-aqueous GG interface on top of which a 5 mL of 0.1 wt % particle suspension in water/EtOH (equal volume) was spread. Subsequent cooling of the GG solution to room temperature jellified the aqueous GG phase, trapping the particles at the interface. Next, the gelled aqueous phase was carefully covered with PDMS elastomer followed by curing at room temperature for 48 h. Before that, the PDMS was manually mixed with the curing agent in a 10:1 ratio and the gas bubbles that evolved during the mixing were vented out via centrifuging the mixture at 4000 rpm for 15 min. The PDMS film with trapped particles was washed several times with water to discard any remaining GG from the particle surface. Next, root-mean square (RMS) roughness of the trapped particles was measured via scanning a single particle using an Asylum MFP- 3D. The images were acquired in tapping mode via probing the sample surface with an Olympus AC240TS-R3 silicon cantilever having a spring constant of 2 N m-1 and a resonance frequency of 70 kHz at ambient conditions. The obtained images were analyzed via an open-source software Gwyddion[4] to obtain RMS roughness. For that, the macroscopic particle curvature was subtracted from the height image to extract the residual surface height profile[5], from which the RMS roughness was determined. A minimum of five particles of each type and at least two regions of 1.5 µm × 1.5 µm area on each particle was analyzed to calculate the RMS values.

To quantify the interfacial deformation (Δh_{max}) around a single particle at air-water interface, we used phase-shift interferometry, where Interferograms were captured on an upright microscope (Nikon FN1) equipped with a 50× Mirau objective and a CMOS image sensor (Nikon DS-Fi3) following an established protocol[6]. The acquired interferograms were analyzed to create a relative height map of the interface around a particle. Along with $\Delta h_{max},$ particle position at and slop of the interface can be extracted from where the corresponding particle contact angle ($\theta_{c,}$), with water sub-phase was calculated using a procedure described in ref [7].

Progression of radial distribution function with particle area fraction

Here, we examine how the radial distribution function ($g(r)$) and the number of nearest neighbors evolves for smooth and concave spheres as we compress the interface (i.e. with increasing particle packing fraction at interface, $\emptyset$). Note that we do not consider the progress of $g(r)$ (and associated nearest neighbors based on the first peak in $g(r)$) for convex rough spheres as the particles are not homogeneously distributed over the imaging area, a prerequisite for $g(r)$ calculation. Fig S5a shows the shift in $g(r)$ pattern for smooth spheres as we increase the $\emptyset$. It is evident that the smooth spheres maintain a constant surface separation ($r=2r_0$, r_0 being the particle radius) throughout the compression till maximum packing when they are in their $r=2r_0$ separation. On the other hand, the surface separation distances of concave rough spheres (Fig S5bc) are way higher than the smooth spheres and they decrease with the barrier closure. For the same surface pressure, the high concave rough spheres seem to have a larger surface separation compared to the low concave rough ones.

Angular correlation function of ellipsoids and its evolution with particle area fraction

The correlation in alignment between neighboring particles can be quantified via the angular correlation function $g_2(r)$, which for smooth and high convex rough ellipsoids at jamming and high concave rough ellipsoids below jamming is shown in Fig S8**.** At large separation, $g_2(r)$ of smooth and high convex ellipsoids show a rapid exponential decay to zero, confirming that particle orientations are not correlated and are randomly distributed. However, $g_2(r)$ profile of high concave rough ellipsoids decay slowly and reach an asymptotic value of ~0.4. This indicates the formation of a nematic phase[8] and that there is a long-range orientational correlation between high concave rough ellipsoids even at $\emptyset$ far below that of smooth and high convex rough ellipsoids.

Next, we discuss the change in the $g_2(r)$ of smooth, high convex rough, and high concave rough ellipsoids at varying $\emptyset$, reported in Fig S9abc. For smooth and convex rough ellipsoids, the pattern is the same which is a rapid exponential decay to zero at large separation, confirming that particle orientations are not correlated and are randomly distributed. Even though the energy minimization imposes a local S–S ordering and thus a $g_2(r)$ value of 1 at close separation, the smooth and convex rough ellipsoids remain globally disordered due to the strong attractive capillary interactions, also shown by Luo et al[9], both experimentally and computationally, for smooth ellipsoids. However, the $g_2(r)$ profile of concave rough ellipsoids changes significantly with $\emptyset$. At low area fractions ($\emptyset$=0.16 and 0.33) the asymptotic value is~0.0, meaning the particles are not correlated at a large separation distance. However, at a small separation distance, they show a similar shape with a first dip that decreases in value and shifts to lower separation distance with increasing $\emptyset$. This dip can be correlated to T–T "flower-like" assembly or triangles in $\emptyset$=0.16 and S–T orientation of splay structures, mostly type *c* (Fig S10), in $\emptyset$=0.33. At high $\emptyset$(=0.49), the type c splay structures transform to type *b* or *a* (as in Fig S10), minimizing the angular difference between particles and increasing the value of that dip, which is also due to the particles aligning with respect to each other in the direction perpendicular to the barrier compression. Now the asymptotic value of ~0.4, which indicates that the orientations of the particles are correlated over a large distance.

An important piece of information about isotropic (I)–nematic (N) phase transition (discussed in the main text) can be extracted from the nature of $g_2(r)$ decay profile. An algebraic decay of the correlation function[10,11] indicates the I–N transition is of Kosterlitz–Thouless (K–T) type[12]. The I–N phase transition observed in our high concave rough ellipsoids is also of K–T type as evidenced from Fig S11 that shows that the $g_2(r)$ decay profile of high concave ellipsoids appear to be algebraic with increasing ∅. The fitting below r= 14 µm is not considered since at very short distances (r<2a, a being the particle semi-major axis) local ordering effects will dominate[11]. The low concave rough ellipsoids demonstrate an analogous orientational correlation dependence on ∅ and thus the result is not reported here.

To get a better understanding of this I–N phase transition, we apply the local kinetic model proposed by Liu et al[13], where Boltzmann distribution can be invoked to extract local free energy from the distribution of the relative angles ($\Delta\theta$) between anisotropic particles at local equilibrium configurations. Fig. S12a shows the probability of the relative angles $P(\Delta\theta)$ between neighboring high concave rough ellipsoidal particles at varying ∅. Obviously, the probability of finding particle pairs in parallel configuration increases while in perpendicular configuration decreases as ∅ increases. According to this model based on Boltzmann statistics[13], $P(\Delta\theta) \propto -\exp(V(\Delta\theta)/k_BT)$, where $V(\Delta\theta)$ is the effective, many-body, potential energy (Gibbs free energy) of the local configuration $\Delta\theta$, k_B is the Boltzmann constant, and T is the temperature. An estimation of $V(\Delta\theta)$ using this kinetic model is shown in Fig. S12b. Here we assume that the concave rough ellipsoids are in their local equilibrium condition by balancing the energetic and entropic interaction at different ∅. From the $V(\Delta\theta)$ plot, the structural origin of the I–N phase transition can be quantitatively addressed by analyzing the change in effective activation barrier, $\Delta V=V_{max}-V_{min}$, with ∅. Certainly, the activation energy barrier between parallel and perpendicular configuration increases with increasing ∅, with the parallel arrangement being the lowest energy state. A similar trend is also observed for low concave rough ellipsoids (results not shown). Therefore, the concave rough ellipsoids tend to be in energy favorable parallel configuration at high interfacial packing, forming *N* phase and compromising their orientational degrees of freedom. The presence of such an energy barrier in the local kinetic model also suggests that the concave rough ellipsoids may undergo two-step glass transition, where orientational glass transition precedes the translational one[14].

Detachment energy of particles from air-water interface

The detachment energy (E_{det}) of a spherical particle from an air-water interface can be described as[15]

$$E_{det} = \pi {r_0}^2 \gamma (1 - |cos\theta_c|^2) \tag{1}$$

Where γ (=72.8 mN/m) is the surface tension at air-water interface. We disregard line-tension since it is relevant only for nano-sized particles[16,17].

Neglecting the interface deformation, the detachment energy of a prolate ellipsoid with its semimajor axis a parallel to the air-water interface can be expressed as[15]

$$E_{det} = 4\pi b^2 G\gamma[\frac{AR}{4G}(1-\bar{h}^2) - cos\theta_c \bar{A}_{p,a}(\bar{h})] \tag{2}$$

Where b is the semi minor axis, $\bar{h} = \frac{h}{b}$ is the dimensionless height and can be approximated as equivalent to $cos\theta_c$, h defines the position of particle's center of mass above the interface, and G is a geometrical aspect factor which for a prolate ellipsoid having AR $(=\frac{a}{b})$ ≥1 takes the following form

$$G = \frac{1}{2} + [\left(\frac{AR}{2\sqrt{1-AR^{-2}}}\right) sin^{-1}(\sqrt{1-AR^{-2}})] \tag{3}$$

and, $\bar{A}_{p,a}(\bar{h})$ represents the fraction of the particle immersed in air and can be described as

$$\bar{A}_{p,a}(\bar{h}) = \frac{AR}{\pi G}\int_0^1 \frac{\sqrt{[1-(1-\bar{h}^2)(1-AR^{-2})x^2](1-\bar{h}^2)}}{tan^{-1}[\frac{1}{\bar{h}}\sqrt{(1-\bar{h}^2)(1-x^2)}]dx} \tag{4}$$

and can change from 0.5 to 0 as the $\bar{h}$ increases from 0 to 1.

In the presence of interface distortion, caused by either surface roughness or shape anisotropy, the term $\gamma\pi(\frac{\Delta h_{max}}{2})^2$ is subtracted [18] from Eq. 1 and 2 to calculate the actual detachment energy of spheres and ellipsoids, respectively. Herer, Δh_{max} is maximum difference in the interface rise and dip assuming quadrupolar distortion as the first surviving mode in the interface distortion[19]. In Fig S13ab, we report the E_{det} normalized by $A_p\gamma$, where $A_p$is the total particle surface area. For spheres, $A_p = 4\pi {r_0}^2$ and for ellipsoids, A_p can be calculated as

$$A_p = 2\pi b^2[1 + \left(\frac{a}{b\sqrt{1-AR^{-2}}}\right) sin^{-1}(\sqrt{1-AR^{-2}}] \tag{5}$$

From Fig S13ab, we can see that the normalized detachment energy ($E_{det}/A_p\gamma$) of the particle at air-water interface decreases with θ_c. If we investigate their actual detachment energy (E_{det}), particularly for spheres in Fig S13c, we see that the smooth spheres have lower E_{det} compared to high convex and concave spheres due to their smaller dimension. Despite that, smooth spheres show higher ϵ_{max} than that of high convex and concave spheres, which implies that the particle position dictated by θ_c, rather than size dependent trapping energy at the interface, dominates their monolayer's mechanical response. Comparing dilational surface viscoelasticty of monolayers of different size PS particles at an oil-water interface, Bykov et al[20] found the monolayer elasticity slightly depends on the particle dimension.

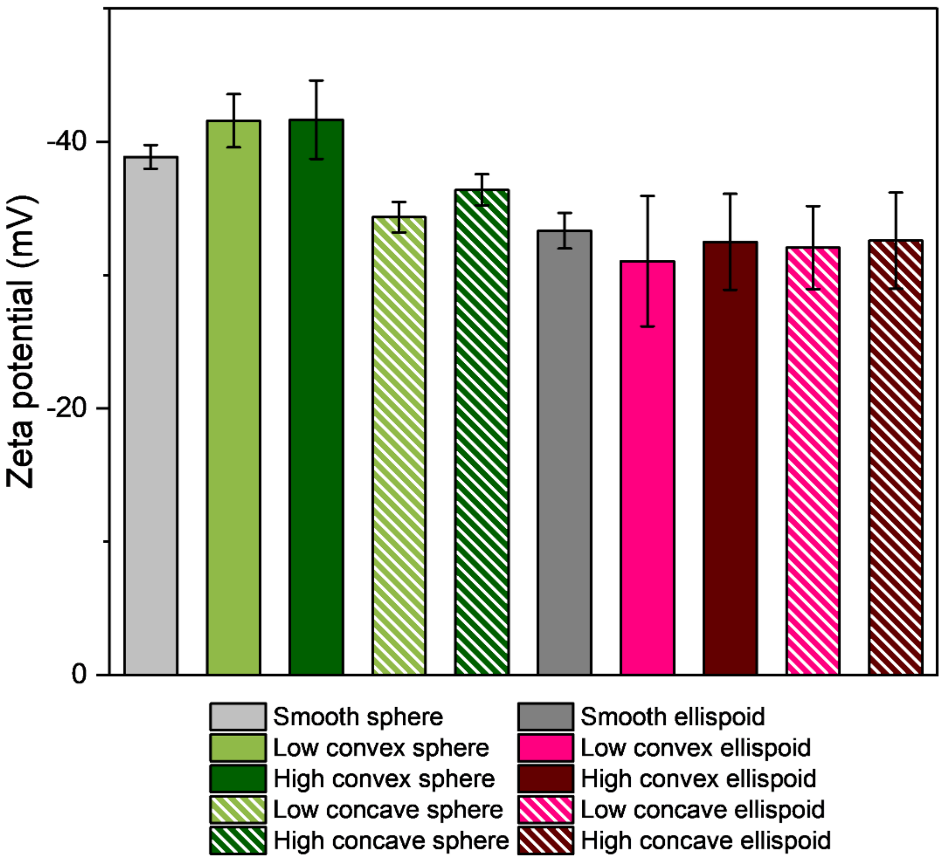

Fig. S1 Surface Zeta potential of spheres and ellipsoids with varying surface morphology (smooth, convex rough, concave roug

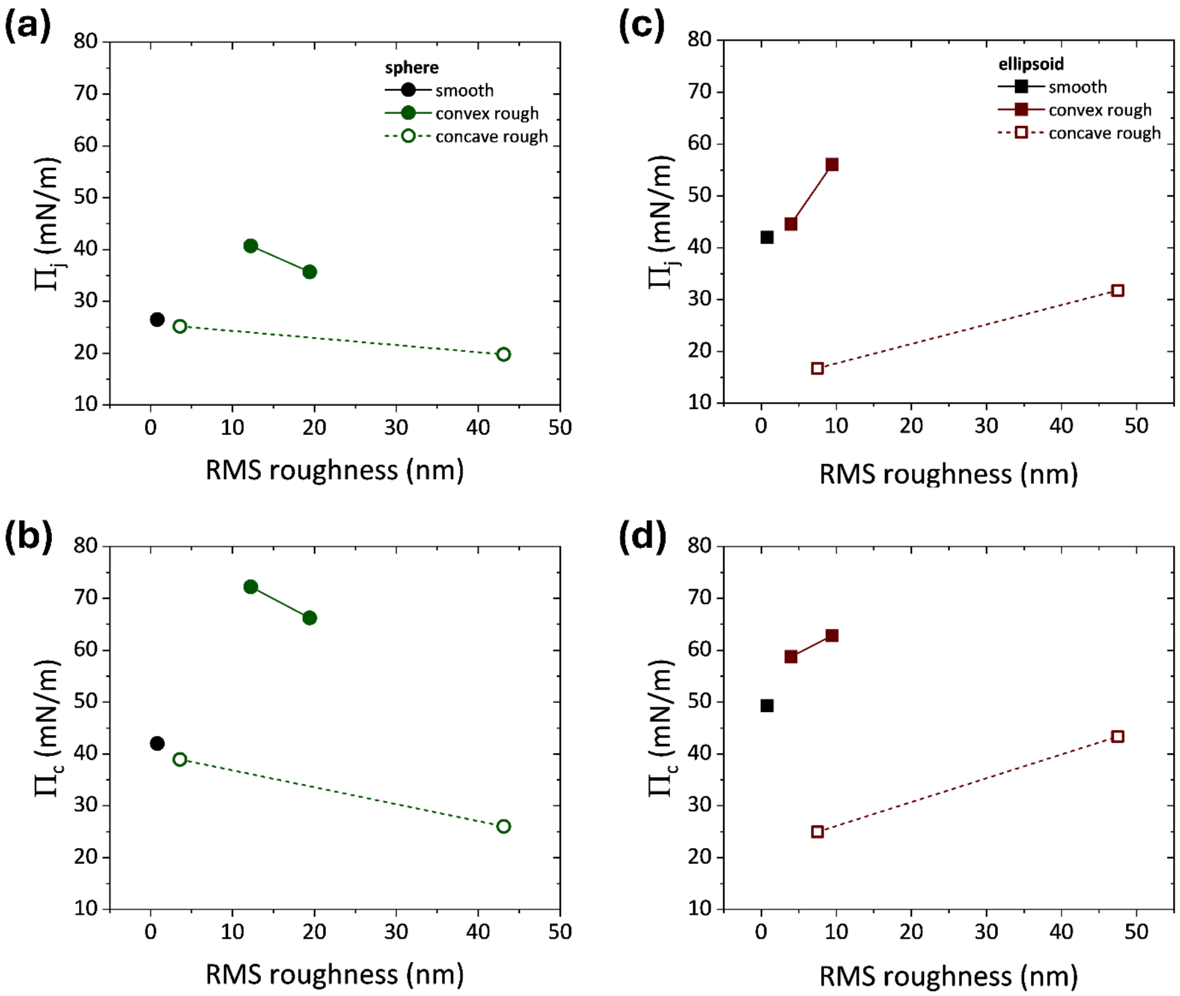

Fig. S2 Surface pressure at jamming (Π_j) and surface pressure at collapse (Π_c) as a function of surface roughness for spheres with varying surface morphology (smooth, convex rough, concave rough) are depicted in a and b, respectively. The corresponding graphs for ellipsoids are shown in c and d.

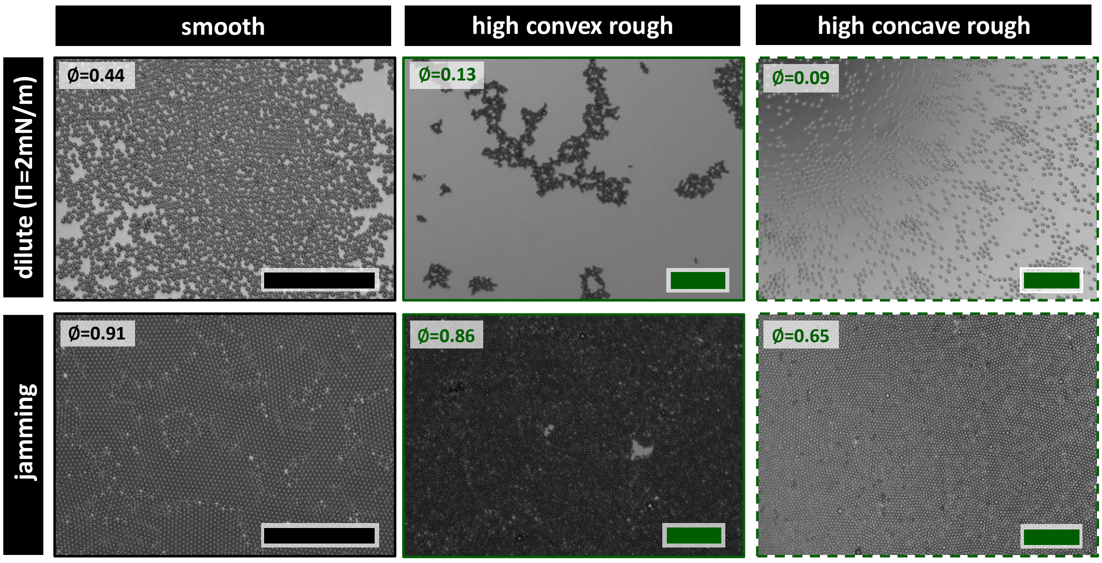

Fig. S3 Optical microscopy images of air-water interface adorned with smooth, high convex rough, and high concave rough spheres at dilute (surface pressure, Π=2mN/m) and jamming condition in conjunction with the respective particle area fraction (Ø) at the interface. All scale bars represent 100 µm.

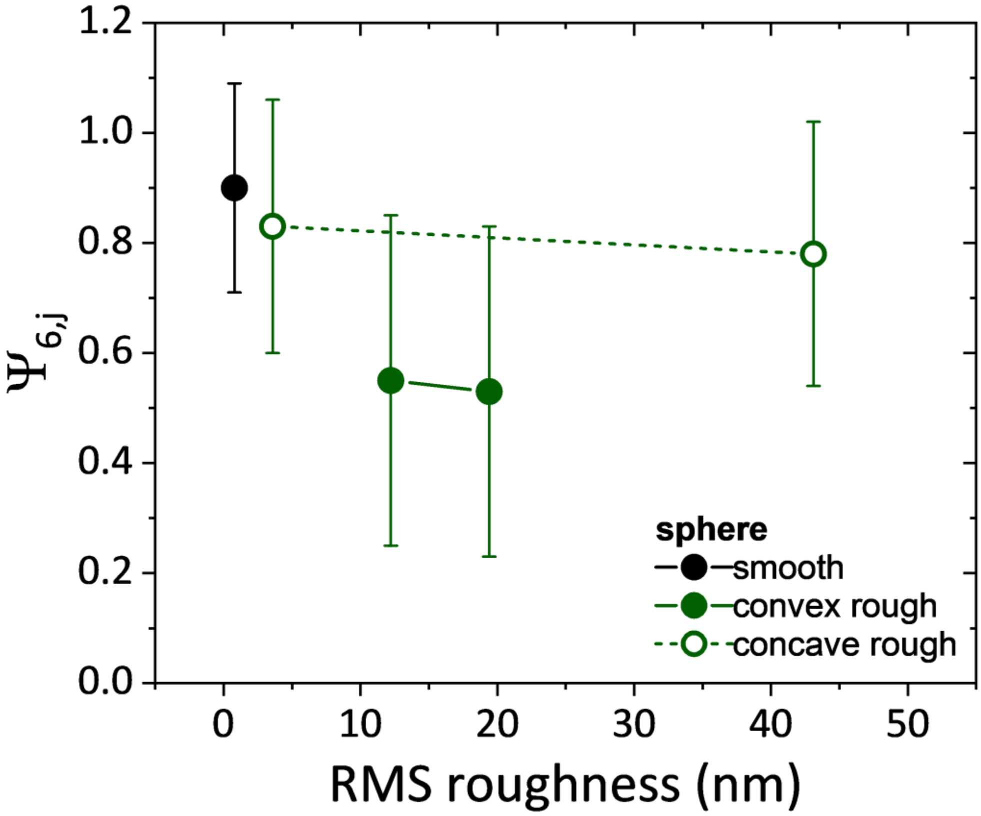

Fig. S4 Hexagonal order parameter of spheres with varying surface morphologies at jamming Ψ_{6j}, as a function of rms roughness.

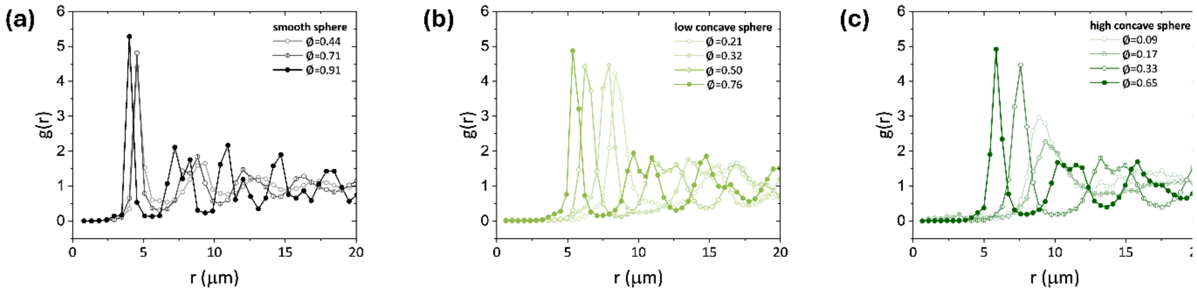

Fig. S5 Progress in radial distribution function *g(r)*with increasing area fraction ∅ for (a) smooth, (b) low concave rough, and (c) high concave rough spheres.

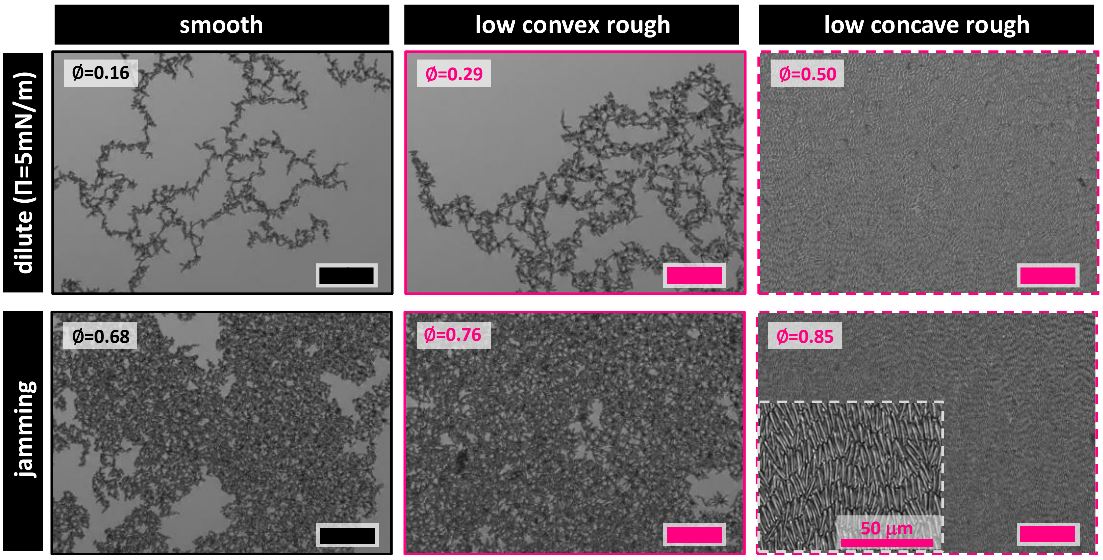

Fig. S6 Optically imaged microstructures at an air-water interface formed by smooth, low convex rough, and low concave rough ellipsoids from dilute (surface pressure, Π=5 mN/m) to jamming condition along with their associated particles area fraction (Ø) at the interface. The inset of the bottom-right image shows nematic liquid crystal structure formed by high concave rough ellipsoids in the direction perpendicular to the monolayer compression. All scale bars represent 100 µm unless otherwise specified.

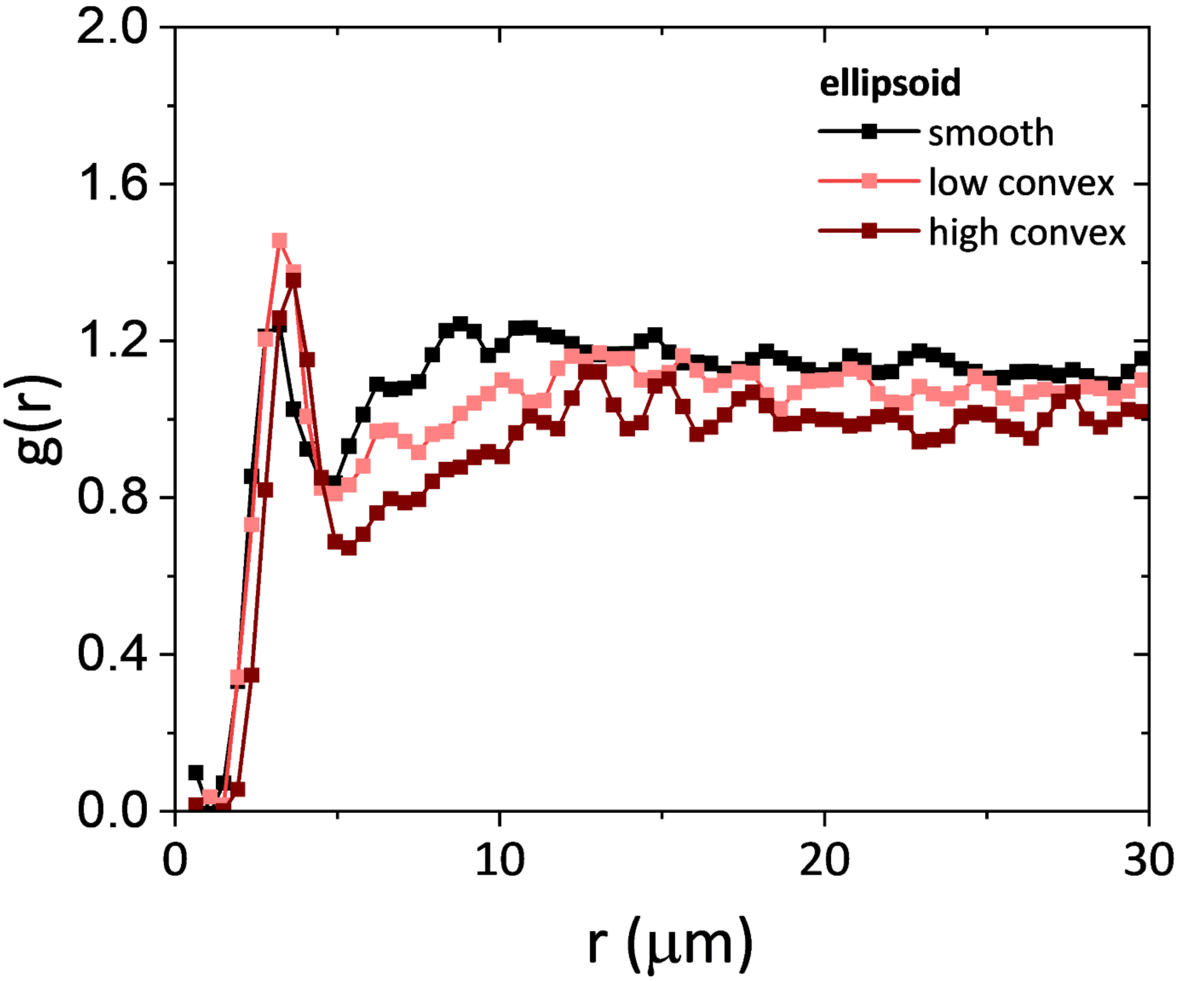

Fig. S7 Radial distribution *g*(*r*) of smooth, low convex rough, and high convex rough ellipsoids at jamming.

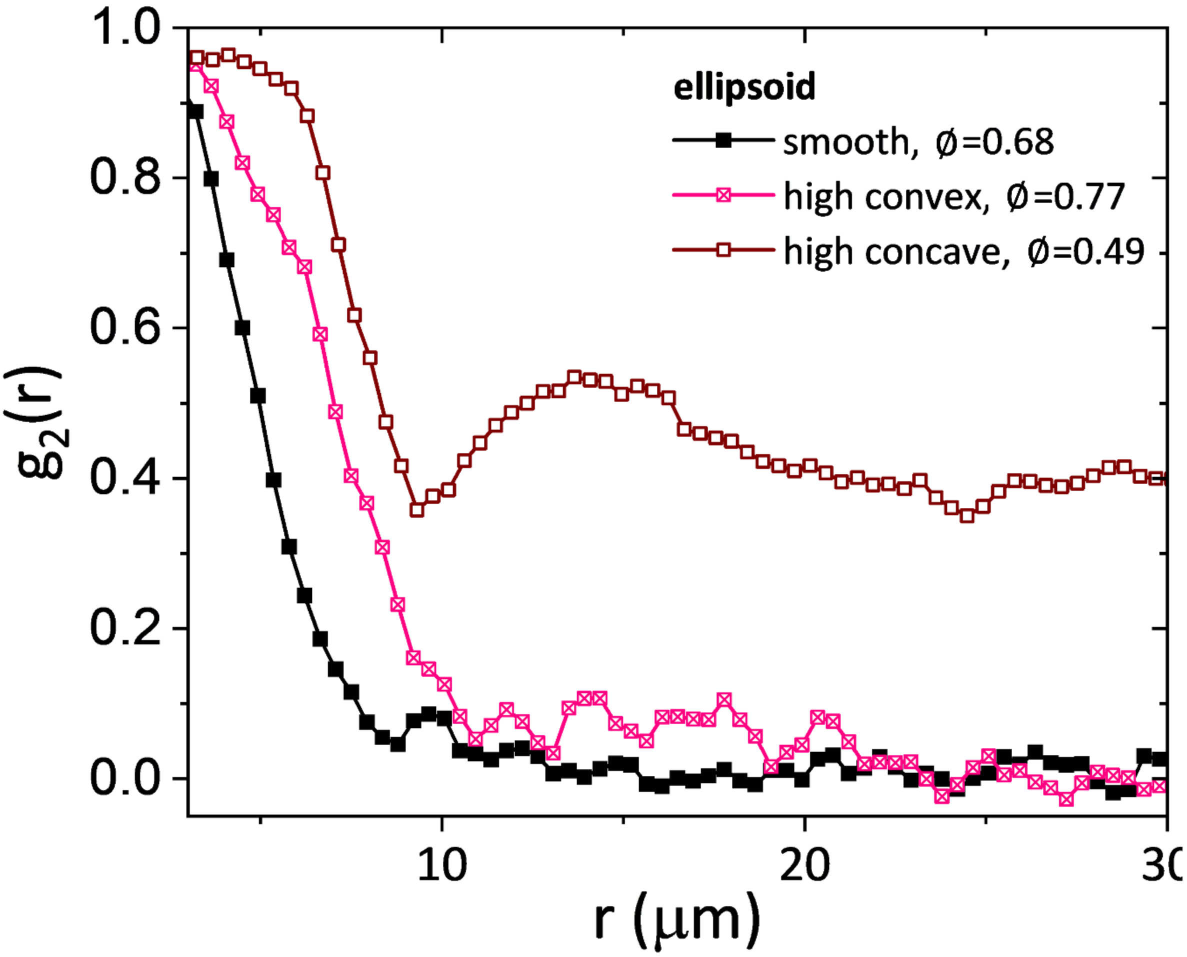

Fig. S8 The orientational correlation function $g_2(r)$ of smooth and high convex rough ellipsoids at jamming and high concave rough ellipsoids at near jamming. A high value of $g_2(r)$ persisting over a large center-to-center particle distance r implies particles exhibit long-ranged orientational correlation.

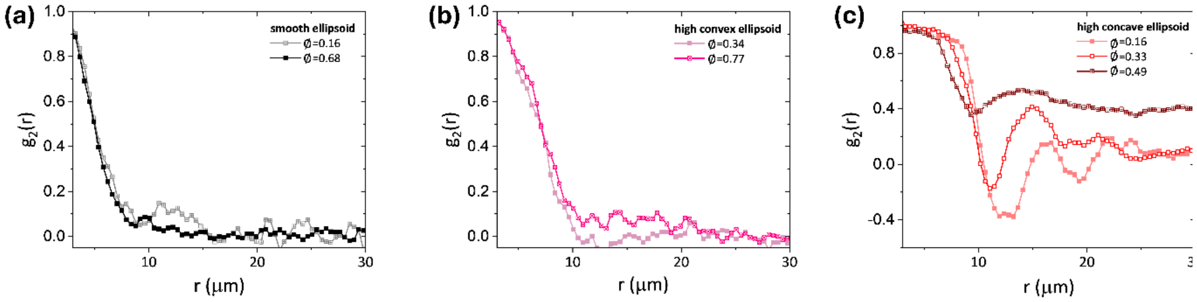

Fig. S9 The change in pattern of orientational correlation function *$g_2(r)$* of (a) smooth, (b) high convex rough, and (c) high concave rough ellipsoids with increasing particle area fraction ∅.

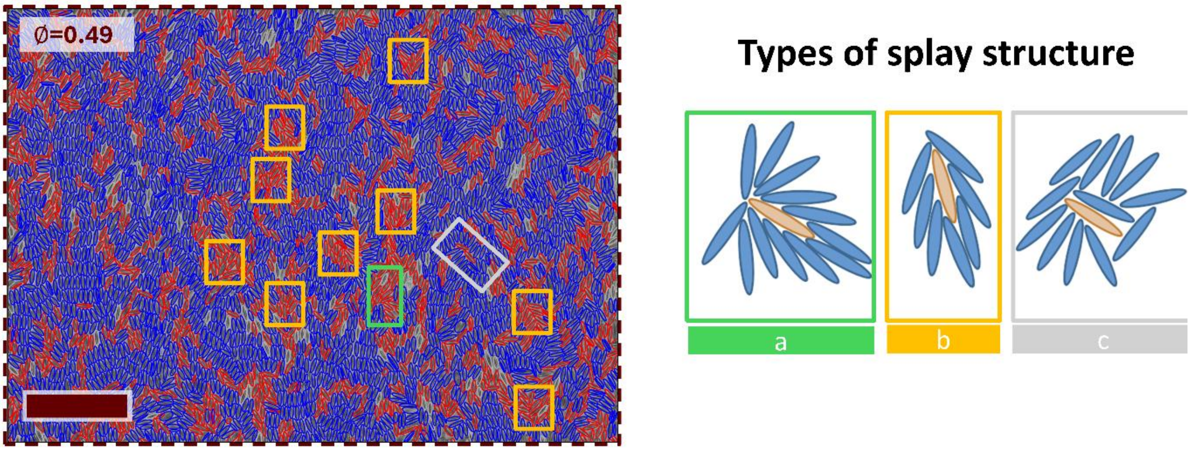

Fig. S10 Formation of different types of splay structures with high number of nearest neighbors in monolayer of high concave rough ellipsoids as the interface approaches jamming. The classification of the splay structures has been adopted from ref [21]. The scale bar represent 100 μm.

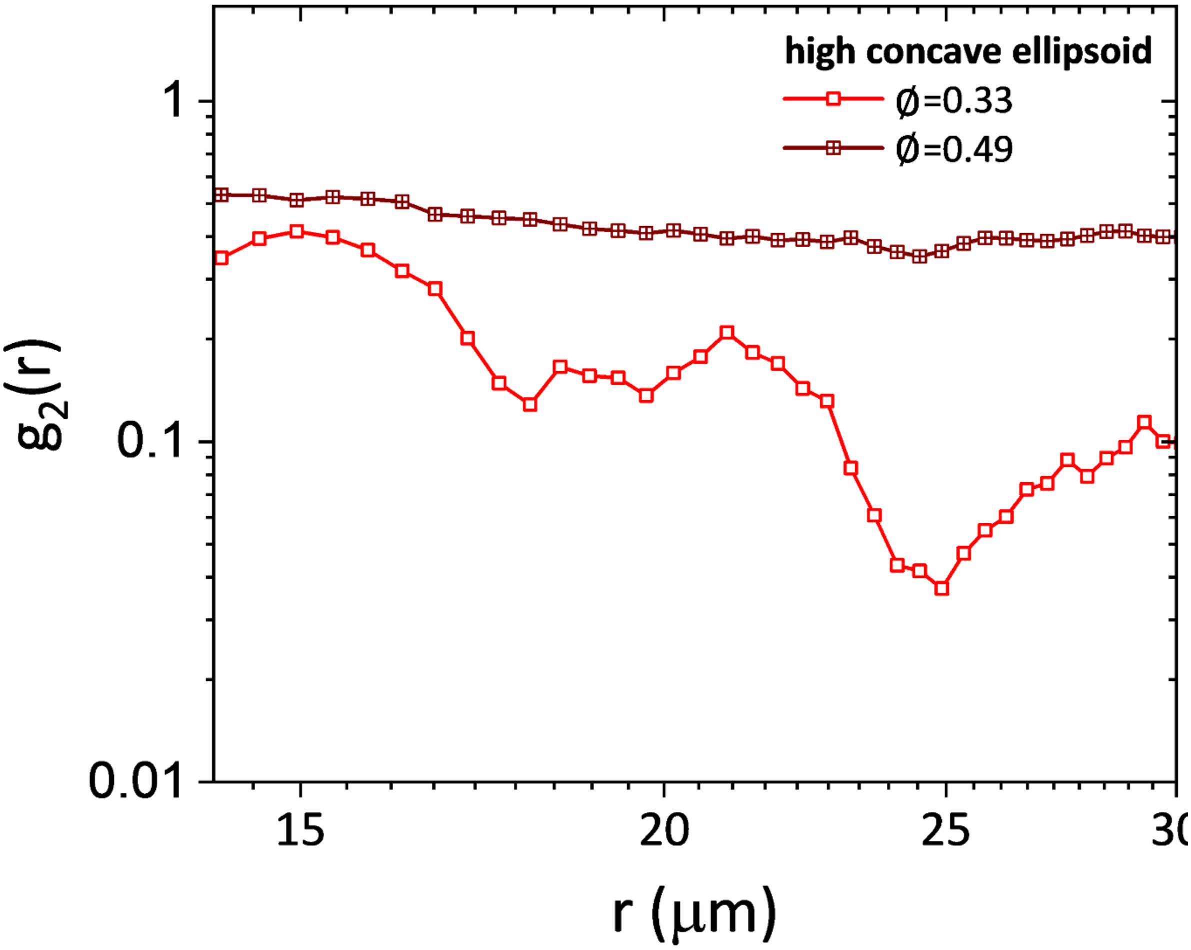

Fig. S11 Log-log plot of $g_2(r)$ displays that the decay profile becomes more algebraic as the particle area fraction Ø increases.

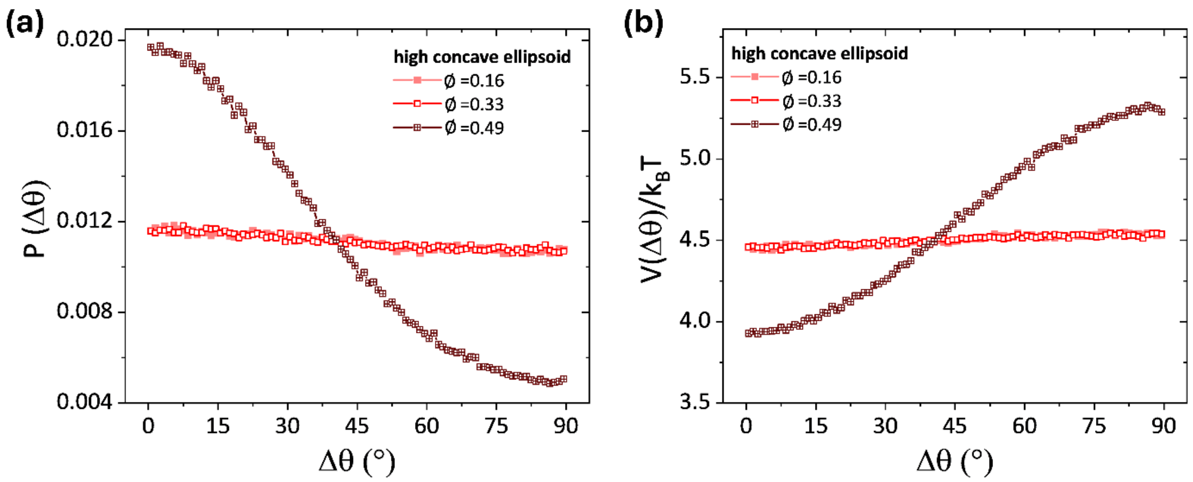

Fig. S12 (a) The probability of the orientational configuration $(\Delta\theta)$ and (b) the associated potential energy $V(\Delta\theta)$, estimated from -$\ln P(\Delta\theta)$, of two neighboring high concave rough ellipsoids at varying ∅.

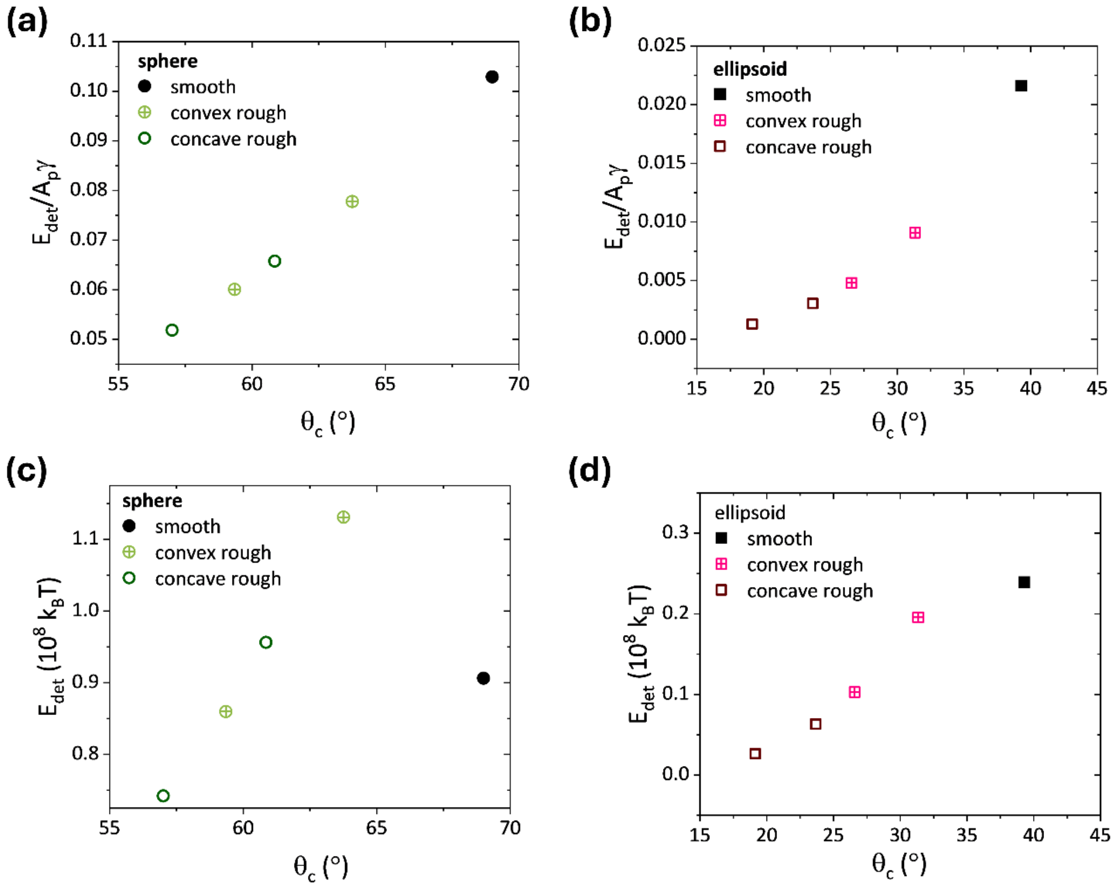

Fig. S13 The normalized energy E_{det} required to detach (a) spherical and (b) ellipsoidal particles with different surface geometry (smooth, convex, and concave) from an air-water interface. E_{det} is normalized by particle surface area $A_p$and surface tension of air-water interface γ. (c) and (d) depicts the E_{det} of spheres and ellipsoids, respectively, before normalization.

Movie S1 (separate file). The video of collapse of low convex spheres at an air-water interface recorded at 1 fps and is sped up 2x. The objective used was a 20x objective on a Nikon FN1 microscope.

Movie S2 (separate file). The video of collapse of low concave spheres at an air-water interface recorded at 1 fps and is sped up 4x. The objective used was a 20x objective on a Nikon FN1 microscope.

Movie S3 (separate file). The video of collapse of smooth ellipsoids at an air-water interface recorded at 1 fps and is sped up 4x. The objective used was a 20x objective on a Nikon FN1 microscope.

Movie S4 (separate file). The video of collapse of high concave ellipsoids at an air-water interface recorded at 1 fps and is sped up 4x. The objective used was a 20x objective on a Nikon FN1 microscope.

SI References

1 S. Trevenen and P. J. Beltramo, *J Colloid Interface Sci*, 2021, **583**, 385–393.

2 J. Schindelin, I. Arganda-Carreras, E. Frise, V. Kaynig, M. Longair, T. Pietzsch, S. Preibisch, C. Rueden, S. Saalfeld, B. Schmid, J. Y. Tinevez, D. J. White, V. Hartenstein, K. Eliceiri, P. Tomancak and A. Cardona, *Nature Methods*, 2012, **9**, 676–682.

3 V. N. Paunov, *Langmuir*, 2003, **19**, 7970–7976.

4 D. Nečas and P. Klapetek, *Central European Journal of Physics*, 2012, **10**, 181–188.

5 M. A. Rahman, T. Turner, H. S. C. Hamilton, L. C. Bradley and P. J. Beltramo, *J Colloid Interface Sci*, 2023, **652**, 82–94.

6 S. Trevenen and P. J. Beltramo, *Review of Scientific Instruments*, 2022, **93**, 73701.

7 M. A. Rahman and P. J. Beltramo, *ACS Applied Materials and Interfaces* , 2024, **16**, 35834–35840.

8 X. Tan, Y. Chen, H. Wang, Z. Zhang and X. S. Ling, *Soft Matter*, 2021, **17**, 6001–6005.

9 A. M. Luo, J. Vermant, P. Ilg, Z. Zhang and L. M. C. Sagis, *J Colloid Interface Sci*, 2019, **534**, 205–214.

10 M. C. Lagomarsino, M. Dogterom and M. Dijkstra, *J Chem Phys*, 2003, **119**, 3535–3540.

11 D. Frenkel and R. Eppenga, *Phys Rev A: atomic, molecular and optical physics*, 1985, **31**, 1776.

12 J. M. Fish and R. L. C. Vink, *Phys Rev E Stat Nonlin Soft Matter Phys*, 2010, **81**, 021705.

13 X. Liu, H. Wang, Z. Zhang, J. M. Kosterlitz and X. S. Ling, *New J Phys*, 2020, **22**, 103066.

14 H. Wang, Z. Zhang and X. S. Ling, *Front Phys*, 2022, **10**, 1043983.

15 G. B. Davies, T. Krüger, P. V. Coveney and J. Harting, *Journal of Chemical Physics*, 2014, **141**, 154902.

16 J. Faraudo and F. Bresme, *Journal of Chemical Physics*, 2003, **118**, 6518–6528.

17 J. M. Y. Carrillo and A. V Dobrynin, *Journal of Physical Chemistry B*, 2010, **114**, 9391–9399.

18 K. Schwenke, L. Isa, D. L. Cheung and E. Del Gado, *Langmuir*, 2014, **30**, 12578–12586.

19 D. Stamou, C. Duschl and D. Johannsmann, *Phys Rev E*, 2000, **62**, 5263.

20 A. G. Bykov, G. Loglio, R. Miller and B. A. Noskov, *Colloids Surf A Physicochem Eng Asp*, 2015, **485**, 42–48.

21 Z. Zheng, R. Ni, F. Wang, M. Dijkstra, Y. Wang and Y. Han, Nat. Commun., 2014, 5, 3829.